# The motion of a falling liquid filament

Diane Henderson[a)]
*William G. Pritchard Fluid Mechanics Laboratory, Department of Mathematics, Penn State University, University Park, Pennsylvania 16802*

Harvey Segur
*Department of Applied Mathematics, University of Colorado, Boulder, Colorado 80309-0526*

Linda B. Smolka
*William G. Pritchard Fluid Mechanics Laboratory, Department of Mathematics, Penn State University, University Park, Pennsylvania 16802*

Miki Wadati
*Department of Physics, University of Tokyo, 7-3-1 Hongo, Bunkyo-ku, Tokyo 113, Japan*

(Received 15 September 1998; accepted 30 November 1999)

When a liquid drop falls from a fluid source with a slow flow rate, it remains attached to the source by an elongating liquid filament until the filament pinches off. For many fluids, this pinch-off occurs first near the end of the filament, where the filament joins to the liquid drop. For other fluids, the filament pinches off at one or more interior points. In this paper, we study the motion of this filament, and we make two points. First, the flow in this filament is *not* that of a uniform jet. Instead, we show experimentally that a different solution of the Navier–Stokes equations describes the motion of this filament before it pinches off. Second, we propose a criterion for the location of the first pinch-off. In particular, we analyze the linearized stability of the exact solution, both for an inviscid fluid and for a very viscous fluid. Our criterion for pinch-off is based on this stability analysis. It correctly predicts whether a given filament pinches off first near its ends or at points within its interior for all of our experimental data. © *2000 American Institute of Physics.* [S1070-6631(00)02403-X]

## I. INTRODUCTION AND MAIN RESULTS

Anyone who has had a leaky water faucet is familiar with the phenomenon of falling liquid drops. A slow flow rate causes a drop to grow to a critical size, after which it falls under the force of gravity; then the process repeats. High-speed imaging now permits observation of this process with a level of detail that was formerly unavailable. The sequence of images in Fig. 1 exhibits the detailed process for a particular liquid. As Fig. 1 shows, the drop starts to fall from the fluid source. As the drop falls, it remains connected to the source by a long, straight liquid filament. This filament grows thinner and longer, until eventually it pinches off, first at the bottom and then at the top of the filament. After pinching off, the elongated filament contracts vertically. Depending on parameter values, the filament may exhibit spatial oscillations before it pinches off, and it may contract into one satellite droplet (as in Fig. 1) or into more than one after pinching off. As we discuss in detail in the following, this sequence of events is typical for many (but not all) fluids.

The process of drop formation, with or without gravity, has been the subject of a great deal of recent research.[1–11] Inspired in part by the results in Ref. 1, most of these papers have focused on the detailed structure of the pinch-off. This paper focuses instead on the motion of the filament visible in Fig. 1, which we call the ''primary filament,'' as it falls under gravity. Our objective is to describe the motion of this falling liquid filament, including: (i) its time-dependent shape and dynamics; (ii) its instabilities; and (iii) whether the filament pinches off near its ends or at interior points.

A nearby but different problem, on the stability of a uniform liquid jet, was studied long ago by Plateau,[12] Rayleigh,[13,14] and Chandrasekhar.[15] People often identify the primary filament of a falling drop with a uniform jet, and an instability on the primary filament is sometimes described in the literature as a ''Rayleigh instability.'' The starting point of our analysis is to deny this identification, because a uniform liquid jet and a falling liquid filament are different. This can be seen in at least two ways.

(a) The axial velocity of a uniform liquid jet is uniform in both time and space. The axial velocity of a falling liquid filament cannot be uniform in time, because it accelerates in a uniform gravitational field. It is not uniform in space either.

(b) As Fig. 1 shows, the radius of the falling filament decreases as the filament grows in length, before pinching off; the radius of a uniform jet is uniform in time. The two motions are different, and neither is a limit of the other.

In Sec. II, we derive an exact solution of the Navier–Stokes equations, in which the radius of the filament decreases in time according to

$$h(t)=\frac{H}{\sqrt{t+t^*}}, \tag{1}$$

[a)]Author to whom all correspondence should be addressed; electronic mail: dmh@math.psu.edu

 

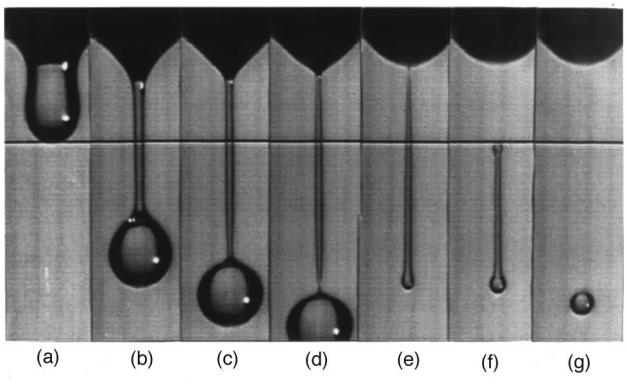


FIG. 1. Evolution of a drop from its formation through the formation of a satellite drop. The resolution is 93.3 $\mu$m/pixel. The size of each image is $0.588\times2.22$ cm$^2$. The times of the images (referenced to times shown in Figs. 2 and 5) are: (a) $-0.0486$ s, (b) 0.0097 s, (c) 0.0167 s, (d) 0.0214 s, (e) 0.0274 s, (f) 0.0330 s, (g) 0.0443 s. The kinematic viscosity ($\nu$) is 0.75 cm$^2$/s. This experiment used fluid A1 in Table I. (*Figure reprinted with permission of the Physics of Fluids.*)

where $\{H,t^*\}$ are arbitrary constants. This form of solution is quite robust: it applies as the filament elongates, for either a viscous or inviscid liquid, with or without surface tension, with or without gravity. It is a simple generalization of a solution found by Frankel and Weihs[16,17] in a very different context. In Sec. II, we show experimentally that (1) describes the behavior of a falling liquid filament until it starts to pinch off. The solution applies to the filament as it appears before, during, and a short while after Fig. 1(b). In Fig. 1(c), the filament has already started necking near the drop. The corresponding velocity and pressure fields are also given in Sec. II.

The motion associated with (1) is subject to the same kind of instability that affects a uniform liquid jet. In Sec. III, we analyze the linearized stability of a falling filament of an inviscid liquid, before it pinches off. The analysis is similar to that done by Rayleigh[13] for an inviscid liquid jet. Our results turn out to be identical to those of Frankel and Weihs.[16] Moreover, the results for a falling filament compare nicely with those of Rayleigh[13] for a uniform jet. One difference is that every uniform inviscid jet is unstable, but some falling inviscid filaments are linearly stable.

In Sec. IV, we analyze the linear stability of a falling filament of a viscous liquid, again before pinch-off. As in the inviscid case, our basic analysis is similar to that of Frankel and Weihs,[17] and it results in a complicated set of integro-differential equations. For a *very viscous liquid*, we show that these integro-differential equations reduce to ordinary differential equations, which can be analyzed in complete detail. For a very viscous liquid, every falling filament is unstable.

A surprising consequence of the two stability analyses in Secs. III and IV is that some falling liquid filaments are *destabilized* by making the fluid more viscous.

The filament shown in Fig. 1 pinches off first near its ends, where it connects to the falling drop at its bottom and to the fluid source at its top. In most of the experiments known to us,[2–5,11] pinch-off occurs first near the ends of the filament, rather than somewhere in the middle. This is called ''end-pinching'' in Ref. 11, where the authors also observe that the filament of a sufficiently viscous fluid can pinch off at interior points, rather than near its ends. We explore this possibility in Sec. V, both experimentally and theoretically. Using the results of the linearized stability analysis from Sec. IV, we propose a criterion to determine whether a given filament, created by a falling liquid drop, will pinch off first near its ends, or at one or more interior points. For all of our experimental data, this criterion correctly predicts whether a given filament pinches off first near its ends or at points within its interior.

## II. THE UNPERTURBED FLOW

We consider axisymmetric motions of an incompressible fluid in a constant gravitational field. The Navier–Stokes equations have the form:[18]

$$\partial_r(ru)+r\partial_z w=0, \tag{2}$$

$$\partial_t u+u\partial_r u+w\partial_z u+\frac{1}{\rho}\partial_r p=\nu\left(\partial_r\left(\frac{1}{r}\partial_r(ru)\right)+\partial_z^2 u\right), \tag{3}$$

$$\partial_t w+u\partial_r w+w\partial_z w+\frac{1}{\rho}\partial_z p=\nu\left(\frac{1}{r}\partial_r(r\partial_r w)+\partial_z^2 w\right)-g, \tag{4}$$

where $\rho$ denotes the density of the fluid, $\nu$ is its kinematic viscosity, $(u,w)$ are velocity components in the $(r,z)$ directions, respectively, and $g$ is the strength of the gravitational field. Note that the $g$ vector points in the $(-z)$ direction. At the center of the filament, where $r=0$, we require

$$u=0, \quad \partial_r w=0, \tag{5}$$

for all $(z,t)$. The outer boundary of the filament is a free surface, which we denote by $r=h(z,t)$. The kinematic boundary condition on $r=h(z,t)$ is

$$\partial_t h+w\partial_z h=u. \tag{6}$$

Requiring that the stress vanish on $r=h(z,t)$ imposes two more conditions:

$$\frac{1}{\rho}p=\frac{2\nu}{\{1+(\partial_z h)^2\}}[\partial_r u+(\partial_z w)(\partial_z h)^2-(\partial_r w+\partial_z u)\times(\partial_z h)]+\frac{\sigma}{\rho}\left[\frac{1}{h\{1+(\partial_z h)^2\}^{1/2}}-\frac{\partial_z^2 h}{\{1+(\partial_z h)^2\}^{3/2}}\right]+\frac{1}{\rho}p_{\mathrm{amb}}, \tag{7}$$

and

$$\nu[(\partial_r u-\partial_z w)(\partial_z h)+\tfrac{1}{2}(\partial_r w+\partial_z u)\{1-(\partial_z h)^2\}]=0, \tag{8}$$

where $\sigma$ is the coefficient of surface tension, $p_{\mathrm{amb}}$ is the pressure of the ambient fluid, and $\{u, w, p,$ and their derivatives$\}$ are evaluated at $r=h(z,t)$.

Figure 1 suggests that after the primary filament has formed and before it has started to pinch off, it evolves so that

$$\partial_t h<0, \quad \partial_z h=0.$$

Before pinch-off, we *define* the primary filament to be the portion of the falling liquid with these properties. It is easy to find solutions to (2)–(8) with these properties. Let $\tau = t + t^*$. Then

$$
\begin{aligned}
w_0(r,z,t) &= \frac{z+z_0}{\tau} - \frac{g}{2}\tau, \\
u_0(r,z,t) &= -\frac{r}{2\tau}, \\
h(z,t) &= h_0(\tau) = \frac{H}{\sqrt{\tau}}, \\
\frac{1}{\rho}p_0(r,z,t) &= \frac{3}{8}\frac{h_0^2(\tau)-r^2}{\tau^2} - \frac{\nu}{\tau} + \frac{\sigma}{\rho h_0(\tau)} + \frac{1}{\rho}p_{\mathrm{amb}},
\end{aligned}
\tag{9}
$$

where $(t^*, H, z_0)$ are arbitrary constants. The reader can verify directly that this is an exact solution of the Navier–Stokes equations for a fluid with a free surface at $r = h_0(\tau)$. For a physical solution, we require $H>0$, $t^*>0$. The solution works equally well for a viscous ($\nu>0$) or inviscid ($\nu=0$) fluid, with or without surface tension ($\sigma$), with or without gravity ($g$).

With $g=0$, (9) describes the motion of a liquid filament that is uniformly extending in the $z$ direction. This special case was previously discovered by Frankel and Weihs,[16,17] who used it to describe the extensional flow of a shaped charge.

The solution in (9) with $g>0$ has a simple interpretation: it describes the free fall of a liquid filament in a uniform gravitational field. To see this, denote the Lagrangian coordinates of a particular fluid particle by $\{r(\tau), z(\tau)\}$. One finds the motion of this fluid particle by solving two ordinary differential equations:

$$
\frac{dz}{d\tau} = w_0 = \frac{z+z_0}{\tau} - \frac{g}{2}\tau, \quad \frac{dr}{d\tau} = u_0 = -\frac{r}{2\tau}.
$$

The result is

$$
z(\tau,\xi) = -\frac{g}{2}\tau^2 + \xi\tau - z_0, \tag{10a}
$$

$$
r(\tau,\zeta) = \frac{\zeta}{\sqrt{\tau}}, \tag{10b}
$$

where $\xi$, $\zeta$ are constants. Equation (10a) is the familiar formula for the position of a particle that is falling in a uniform gravitational field. The constant of integration, $\xi$, can be interpreted as the vertical velocity of the particle at $\tau=0$.

Equation (10b) also has a simple interpretation. All of the fluid particles in Fig. 1 began their motion at the fluid source. The particles lower in the filament are further from the source, so they have been falling longer and are falling faster than those above. Therefore $\partial_z w>0$, as one confirms directly from (9). Conservation of mass requires that the filament balance this vertical stretching by contracting radially. This radial contraction accounts for the time dependence seen in both (10b) and (1).

Thus, the solution in (9) and (1) has a simple explanation: free fall. We show next that it describes the observed motion of actual filaments. To test (1), we conducted several experiments like that shown in Fig. 1, using a variety of liquids. The experimental apparatus was described in detail in Ref. 5; additional information can be found in Appendix A. In each experiment we measured the thickness, $2h$, of the liquid filament at a fixed $z$ location as a function of time. The constants $\{H, t^*\}$ for that experiment were determined by applying (1) to two points in the resulting time series. (See Appendix A for more detail.) For each experiment, we used data for the time interval over which (1) applies (i.e., for which $\partial_z h = 0$ in that experiment). We show experimentally in Sec. V that this time interval increases with increasing viscosity of the fluid.

Figure 2 shows the results for eight experiments, in which we varied not only the fluid properties (viscosity and surface tension), but also the external parameters of the experiment (flow rate and orifice size). The parameters for these experiments are listed in Table I in Appendix A. The data are graphed with $h\sqrt{t+t^*}$ as a function of $t$, to determine whether the data for each experiment lie on a horizontal line, as predicted by (1). They do, with noticeable oscillations. The horizontal lines shown in Fig. 2 correspond to the best value of $H$ for the particular experiment. Thus, Fig. 2 shows that for a wide range of fluid and experimental parameters, there are values of $\{H, t^*\}$ such that (1) models well the radial contraction of falling liquid filaments. In the experiments shown in Fig. 2, the radius of the filament typically contracted by a factor of more than 2 during the time interval shown, so Rayleigh's model of a uniform jet cannot describe these filaments. On the other hand, these data do not exclude the possibility of some other model in which the radius of the filament also contracts, like that in Ref. 19.

Note that the data in each experiment in Fig. 2 exhibit small oscillations about the value of $H$ for that experiment. This might be evidence of fluid instability, which we discuss in Sec. III.

Before doing so, we mention a variation on (1) and (9). For $t<T$, the Navier–Stokes equations also admit a solution in which

$$
h(t) = \frac{K}{\sqrt{T-t}};
$$

the other variables in (9) are unchanged if we reinterpret: $\tau = t - T$ in (9). This solution is as robust as that in (9): it applies for either a viscous or inviscid fluid, with or without surface tension, with or without gravity. In (9), the filament stretches vertically as it falls; here the filament contracts vertically and grows radially. The solution in (9) describes the motion of the filament before it pinches off. It is tempting to speculate that this second solution might describe the motion of the filament after it pinches off, as it contracts into one or more droplets [i.e., in frames (e) and (f) of Fig. 1]. Unfortunately, we have no experimental evidence to support this speculation.

## III. STABILITY OF AN INVISCID LIQUID FILAMENT

The viscosity of the fluid does not affect the velocity fields in (9), but it affects the stability of the solution. In this

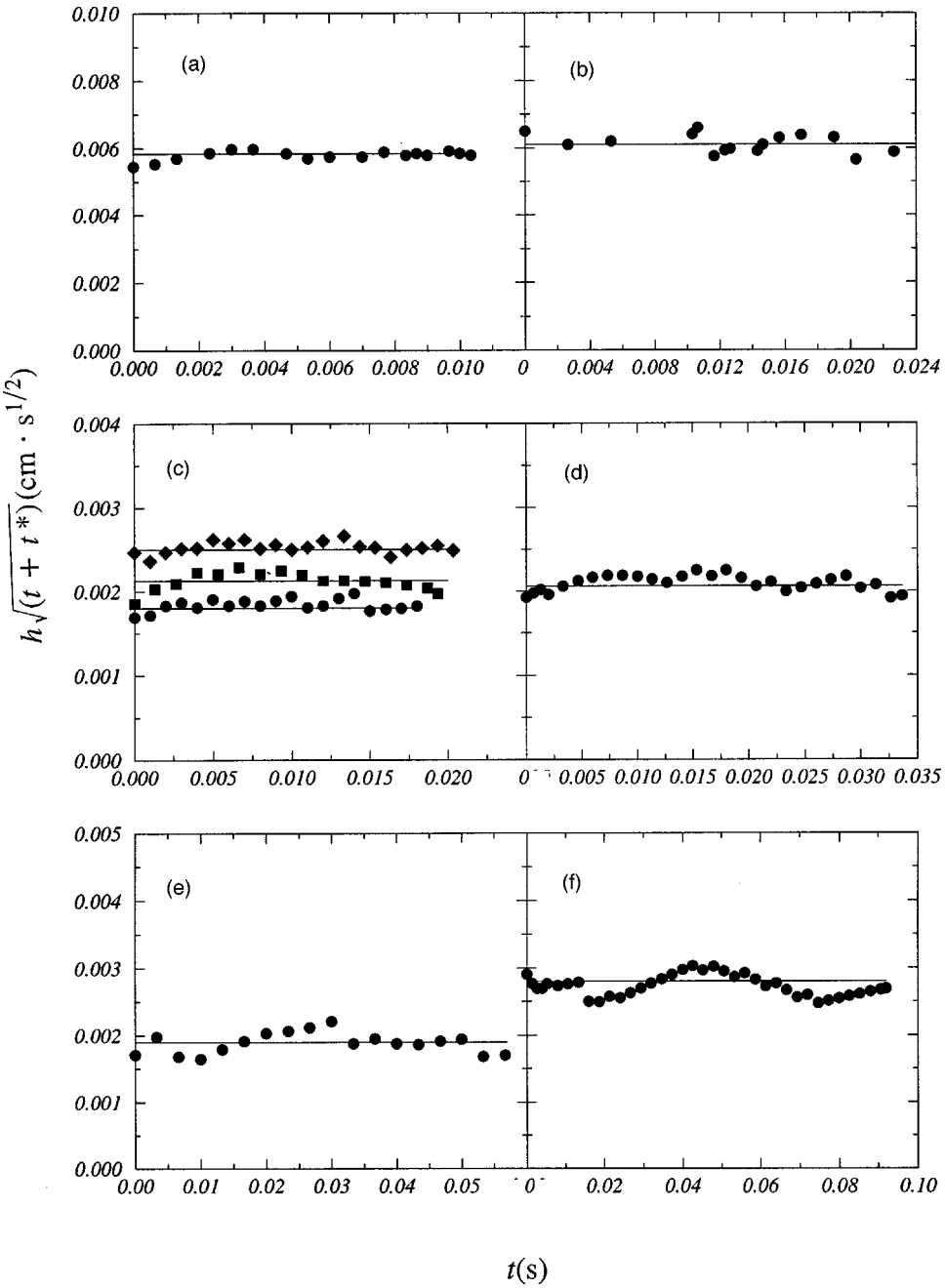


FIG. 2. The quantity $h\sqrt{t+t^*}$ vs $t$ for eight experiments. Fluid viscosities, surface tensions, flow rates, and orifice sizes are listed in Table I of Appendix A. Symbols represent measurements. The horizontal lines represents the values of $H$. (Values of $\{H,t^*\}$ for each experiment are given in Table III of Appendix A.) (a) Fluid A1; (b) fluid A2; (c) fluid B1 (circle), fluid B2 (square), fluid B3 (triangle); (d) fluid C; (e) fluid D; (f) fluid E.

section, we analyze the linearized stability of (9) for an inviscid fluid. The first step is to perturb around the solution in (9), substitute into (2)–(7) with $\nu=0$, and keep only linear terms in the perturbed variables. The result is a set of linearized equations for the perturbed variables, $\{u_1(r,z,\tau), w_1(r,z,\tau), p_1(r,z,\tau), h_1(z,\tau)\}$. For example, the linearized forms of (3) and (4) are (for $0<r<h_0(\tau)$)

$$\partial_t u_1 - \frac{r}{2\tau}\partial_r u_1 - \frac{u_1}{2\tau} + \left(\frac{z+z_0}{\tau} - \frac{g}{2}\tau\right)\partial_z u_1 + \frac{1}{\rho}\partial_r p_1 = 0, \tag{11a}$$

$$\partial_t w_1 - \frac{r}{2\tau}\partial_r w_1 + \frac{w_1}{\tau} + \left(\frac{z+z_0}{\tau} - \frac{g}{2}\tau\right)\partial_z w_1 + \frac{1}{\rho}\partial_z p_1 = 0. \tag{11b}$$

Define the vorticity of the linearized flow:

$$\omega_1 := \partial_r w_1 - \partial_z u_1. \tag{12}$$

It follows from (11a) and (11b) that

$$\partial_\tau \omega_1 - \frac{r}{2\tau}\partial_r \omega_1 + \left(\frac{z+z_0}{\tau} - \frac{g}{2}\tau\right)\partial_z \omega_1 + \frac{\omega_1}{2\tau} = 0. \tag{13}$$

The governing equations for this linearized flow are more complicated than those for many stability analyses, including those of Rayleigh's jet, because of the variable coefficients in (11) and (13). Some of this difficulty can be overcome by changing variables. Let $\{r,z,\tau\}\to\{\zeta,\xi,\tau\}$ according to

$$\zeta = r\sqrt{\tau}, \quad \xi = \frac{z+z_0}{\tau} + \frac{g}{2}\tau, \tag{14}$$

TABLE I. Fluid and experimental parameters.

| Fluid | Viscosity ($cm^2/s$) | Density ($g/cm^3$) | Sur ten (dyn/cm) | Flow rate (s/drop) | Flow rate (ml/s) | Orifice radius (cm) |
|---|---|---|---|---|---|---|
| A1 | 0.75 | 0.968 | 36.7 | 90.8 | $1.09E-3$ | 0.192 |
| A2 | 0.79 | 0.968 | 36.7 | 2.9 | $1.86E-2$ | 0.192 |
| B1 | 0.98 | 0.928 | 21.5 | 30.5 | $5.3E-4$ | 0.176 |
| B2 | 1.02 | 0.928 | 21.5 | 34.1 | $5.0E-4$ | 0.192 |
| B3 | 0.96 | 0.928 | 21.5 | 30.4 | $6.06E-4$ | 0.216 |
| C | 2.13 | 0.968 | 22.0 | 30.3 | $5.3E-4$ | 0.192 |
| D | 4.93 | 0.966 | 21.7 | 26.6 | $6.83E-4$ | 0.216 |
| E | 10.97 | 0.955 | 22.0 | 29.5 | $6.39E-4$ | 0.216 |

so that

$$\partial z = \frac{1}{\tau}\partial_\xi, \quad \partial_r = \sqrt{\tau}\partial_\zeta,$$

$$\partial_\tau \to \frac{r}{2\sqrt{\tau}}\partial_\zeta + \left(-\frac{z+z_0}{\tau^2} + \frac{g}{2}\right)\partial_\xi + \partial_\tau.$$

Comparing (14) with (10) shows that the new variables can be interpreted as Lagrangian-like coordinates of the unperturbed flow. This identification was first made in Ref. 16. Moreover, the effect of gravity disappears when the linearized equations are written in these variables, and the linearized equations here become identical with those in Ref. 16. Hence we may simply state the main points of the resulting analysis.

In terms of the variables in (14), the solution of (13) is

$$\omega_1(\zeta,\xi,\tau) = \sqrt{\frac{\tau_0}{\tau}}\,\omega_1(\zeta,\xi,\tau_0). \tag{15}$$

If the fluid starts from rest, as it does in the experiment shown in Fig. 1, then its vorticity vanishes initially (*i.e.*, at $\tau=\tau_0$), and (15) guarantees that the motion remains irrotational for $\tau \geqslant \tau_0$. We now assume that the linearized motion of the inviscid fluid is *irrotational*, so $\omega_1 \equiv 0$. Then the linearized velocities can be represented in terms of a velocity potential, which satisfies a form of Laplace's equation. It follows that for an infinitely long filament, the velocity field has the form

$$u_1(\zeta,\xi,\tau) = \int_0^\infty I_1\left(\frac{m\zeta}{\tau^{3/2}}\right)[A(m,\tau)\cos(m\xi) + B(m,\tau)\sin(m\xi)]\,dm, \tag{16a}$$

$$w_1(\zeta,\xi,\tau) = -\int_0^\infty I_0\left(\frac{m\zeta}{\tau^{3/2}}\right)[A(m,\tau)\sin(m\xi) - B(m,\tau)\cos(m\xi)]\,dm. \tag{16b}$$

The free surface is given by

$$h_1(\xi,\tau) = \frac{1}{\sqrt{\tau}}\int_0^\infty [C(m,\tau)\sin(m\xi) + D(m,\tau)\cos(m\xi)]\,dm; \tag{17}$$

and there is a corresponding representation $p_1(\zeta,\xi,\tau)$. In (16) and (17), $\{A,B,C,D\}$ are functions to be determined, and $\{I_0(\chi), I_1(\chi)\}$ are modified Bessel functions. The filament is unstable if $h_1(\xi,\tau)$ grows relative to $h_0(\tau)$. Because of the form of (17), the filament is unstable if either $C(m,\tau)$ or $D(m,\tau)$ grows with $\tau$. The governing equation for $C(m,\tau)$ turns out to be

$$\frac{d}{d\tau}\left(\sqrt{\tau}\frac{I_0(\chi)}{I_1(\chi)}\frac{dC}{d\tau}\right) - \left[\frac{\sigma\tau^{3/2}}{\rho H^3}(1-\chi^2) - \frac{3}{4\tau^2}\right]\chi\sqrt{\tau}C = 0, \tag{18}$$

where

$$\chi = \frac{mH}{\tau^{3/2}} \tag{19}$$

is a dimensionless, time-dependent, axial wave number. $D(m,\tau)$ also satisfies (18). Therefore, for each fixed $m$, (18) determines the stability/instability of the corresponding wave mode, for an invisicid fluid.

*Comment:* An equation equivalent to (18) was first derived in Ref. 16, without the restriction to axisymmetric modes. Those authors showed from their more general equation that only the axisymmetric modes can be unstable, so (18) contains all of the unstable modes if $g=0$. It is not difficult to show that their conclusion also holds if $g>0$, and that the analysis presented here captures all the linearized instabilities of (9).

*Comment:* The analysis leading to (18) assumed that the filament is infinitely long. For a filament of finite length, the integrals in (16) and (17) should be replaced by discrete sums, and $m$ should be restricted to a countable set of nonnegative values. These changes do not affect (18), which applies to each relevant mode ($m$).

Note that if $\tau>0$ and $m>0$, then $\chi>0$ and $(\sqrt{\tau}I_0(\chi)/I_1(\chi))>0$. Therefore (18) has the standard form of a Sturm–Liouville equation.[20] In this form, it is easy to identify the stable and unstable modes: (18) necessarily has a growing (i.e., unstable) solution if

$$\left[\frac{\sigma\tau^{3/2}}{\rho H^3}(1-\chi^2) - \frac{3}{4\tau^2}\right] > 0. \tag{20}$$

Conversely, neither solution of (18) can grow in $\tau$ if the quantity in (20) is strictly negative. This is the condition for the filament to be linearly stable.

These inequalities provide the criteria for the linear stability of an inviscid liquid filament as it falls. Equations (18)–(20) are the main results of this section, so we now examine them in detail.

(1) The gravitational constant, $g$, does not appear in (18). Thus, the flow in (9) is a result of gravity, but the inviscid stability of that flow does not depend on gravity.

(2) We may write (20) in terms of a conventional wave number, as follows. Let $k=m/\tau$; then $k$ is an ordinary, dimensional wave number of a spatial oscillation in the $z$ direction. From (19) and (9),

$$\chi=\frac{mH}{\tau^{3/2}}=kh_0(\tau). \tag{21a}$$

Therefore, the set of linearly unstable wave numbers for a falling filament of an inviscid fluid is given by (20), or equivalently by

$$1-(kh_0)^2-\frac{3}{4}\frac{\rho(h_0)^3}{\sigma\tau^2}>0. \tag{21b}$$

Note that (21b) can only hold for $(kh_0)$ small enough, so this is a long-wave instability, like Rayleigh's instability for a uniform jet.

(3) We may compare the results for a falling inviscid filament to Rayleigh's[13] results for an inviscid jet of (constant) radius $a$. Rayleigh found that a jet is always unstable, with a set of unstable wave numbers given by

$$1-(ka)^2>0. \tag{22}$$

Thus, the results for an inviscid falling filament differ from those for an inviscid jet in three ways.

(i) The constant radius of the jet ($a$) must be replaced by the time-dependent radius of the filament $[h_0(\tau)]$.

(ii) The constant growth rate of the instability of the jet must be replaced by the variable growth rate of the instability of the filament, obtained by integrating (18).

(iii) An extra term in (21b), $\frac{3}{4}[\rho(h_0)^3/\sigma\tau^2]$, has no counterpart in (22). This term arises from the radial pressure gradient of the falling filament, which makes the filament more stable than a jet of the same liquid and the same (instantaneous) radius.

(4) A consequence of the additional term in (21b) is that a filament of sufficiently large radius is linearly stable: this occurs if

$$\frac{3}{4}\frac{\rho(h_0)^3}{\sigma\tau^2}>1. \tag{23}$$

As $\tau$ increases, $h_0(\tau)$ decreases, so eventually (23) fails; every filament becomes unstable eventually. Even so, some filaments enjoy a time interval of stability, whereas uniform liquid jets are always unstable.

(5) In Ref. 13, Rayleigh introduced the concept of the ''most unstable wave number.'' This is the wave number of the fastest growing wave mode, so it is the wave number that one is liable to observe in an experiment. For a falling liquid filament, (18) is time dependent, so the ''most unstable wave number'' changes in time. Thus, the process by which a falling liquid filament ''selects'' a particular wave number is more complicated than it is for a liquid jet. This point was emphasized by Frankel and Weihs,[16] who integrated an equation equivalent to (18) numerically.

## IV. STABILITY OF A VISCOUS LIQUID FILAMENT

The linearized stability analysis for a viscous liquid is more complicated than that for an inviscid liquid. We carry this analysis to completion only for a ''very viscous'' liquid, which is defined precisely in (35). In this limit, the main result is that the set of unstable wave numbers is given by (43). The growth of these unstable modes can be found by integrating (40) numerically. In Sec. V, we use these results to predict whether a given filament pinches off first near its ends or in the interior of the filament.

A similar analysis was given in Ref. 17. Those authors did not restrict their attention to ''very viscous'' liquids, so their results are less explicit than those obtained here.

### A. The linearized equations

In terms of the variables defined in (14), the linearized equations for the evolution of the perturbed quantities with $\nu>0$ are as follows.

For $0<\zeta<H$,

$$\partial_\zeta(\zeta u_1)+\tau^{-3/2}\zeta\partial_\xi w_1=0, \tag{24a}$$

$$\partial_\tau u_1-\frac{u_1}{2\tau}+\frac{\sqrt{\tau}}{\rho}\partial_\zeta p_1=\nu\tau\left(\partial_\zeta^2 u_1+\frac{1}{\zeta}\partial_\zeta u_1-\frac{u_1}{\zeta^2}\right)+\frac{\nu}{\tau^2}\partial_\xi^2 u_1, \tag{24b}$$

$$\partial_\tau w_1+\frac{w_1}{\tau}+\frac{1}{\rho\tau}\partial_\xi p_1=\nu\tau\left(\partial_\zeta^2 w_1+\frac{1}{\zeta}\partial_\zeta w_1\right)+\frac{\nu}{\tau^2}\partial_\xi^2 w_1, \tag{24c}$$

at $\zeta=0$,

$$u_1=0,\quad \partial_\zeta w_1=0, \tag{24d}$$

at $\zeta=H$,

$$\partial_\tau h_1+\frac{h_1}{2\tau}=u_1|_{\zeta=H}, \tag{24e}$$

$$\frac{1}{\rho}p_1|_{\zeta=H}=\frac{3}{4}\frac{Hh_1}{\tau^{5/2}}-\frac{\sigma}{\rho}\frac{\tau h_1}{H^2}-\frac{\sigma}{\rho\tau^2}\partial_\xi^2 h_1+2\nu\sqrt{\tau}\partial_\zeta u_1|_{\zeta=H}, \tag{24f}$$

$$\nu\left[-\frac{3}{\tau^2}\partial_\xi h_1+\sqrt{\tau}\partial_\zeta w_1+\frac{1}{\tau}\partial_\xi u_1\right]=0. \tag{24g}$$

Again, note that the gravitational constant $\{g\}$ does not appear in (24), so $\{g\}$ does not affect the linear stability of the system.

The vorticity equation follows from (24b) and (24c):

$$\partial_\tau\omega_1+\frac{\omega_1}{2\tau}=\nu\tau\left(\partial_\zeta^2\omega_1+\frac{1}{\zeta}\partial_\zeta\omega_1-\frac{\omega_1}{\zeta^2}\right)+\frac{\nu}{\tau^2}\partial_\xi^2\omega_1. \tag{25}$$

For a viscous liquid ($\nu>0$), this is a partial differential equation, so it needs boundary conditions. They are as follows.

(i) The vorticity should be bounded for all $\xi$.
(ii) From (24d), $\omega_1$ vanishes at $\zeta=0$.
(iii) From (24e) and (24g), one shows that

$$\omega_1|_{\zeta=H} = -2\partial_\tau\left(\frac{1}{\tau}\partial_\xi h_1\right). \tag{26}$$

The vorticity equation, (25), is essentially a diffusion equation; its solution decays in time. Even so, (26) shows that motion of the free surface can create *new* vorticity at this surface. The competition between these two processes (i.e., creation and decay of vorticity) determines the strength of the rotational velocity field. Thus, the velocity field in the viscous problem consists of three parts:

(1) an irrotational velocity field, analogous to that in the inviscid problem;
(2) a rotational velocity field, generated by the *original* vorticity distribution of the fluid (at $\tau=\tau_0$), which decays as $\tau\to\infty$;
(3) another rotational velocity field, generated by new vorticity created at the free surface.

### B. Three velocity fields

The *irrotational* velocity field is identical in form to that in (16). It is one part of the velocity field in the viscous problem.

Because (25) is a diffusion equation, the *original* vorticity decays in time. The corresponding velocity fields also decay in time. Moreover, this part of the velocity field creates no new instabilities, beyond those already seen in Sec. III. Therefore, to simplify the analysis as much as possible, we now *assume* that the original velocity field is *irrotational*, so the original vorticity vanishes (at $\tau=\tau_0$). Then it follows that this (second) part of the velocity field also vanishes, for $\tau\geqslant\tau_0$.

Finally, consider the vorticity *generated* by motion of the free surface, according to (26). This vorticity satisfies a nonhomogeneous equation, with the forcing occurring at the free boundary. One way to find this vorticity is to find solutions of the homogeneous problem, then to use variation of parameters to build a Green's function of the nonhomogeneous problem (e.g., see Chap. 8 of Ref. 21). Here we simply list the main ingredients in this construction, and the final result. First, represent the right-hand side of (26) by

$$-2\partial_\tau\left(\frac{1}{\tau}\partial_\xi h_1\right) = \frac{1}{\sqrt{\tau}}\int_0^\infty [P(m,\tau)\cos(m\xi) + Q(m,\tau)\sin(m\xi)]\,dm. \tag{27}$$

With $h_1(\xi,\tau)$ represented as in (17), the relations between the coefficients are

$$\frac{P(m,\tau)}{\sqrt{\tau}} = -2m\partial_\tau(\tau^{-3/2}C(m,\tau)),$$
$$\frac{Q(m,\tau)}{\sqrt{\tau}} = +2m\partial_\tau(\tau^{-3/2}D(m,\tau)). \tag{28}$$

We now *assume* that initially, at $\tau=\tau_0$, $P(m,\tau_0)=0=Q(m,\tau_0)$, and we use this fact in Appendix B. Then make use of the identity (p. 111 of Ref. 22),

$$\frac{\zeta}{H} = \sum_{k=1}^{\infty}\frac{2}{n_k H J_2(n_k H)}J_1(n_k\zeta), \quad 0\leqslant\zeta<H, \tag{29a}$$

where $\{n_k H\}$ denote the zeroes of $J_1(x)$,

$$J_1(n_k H)=0, \quad k=1,2,3,..., \tag{29b}$$

so $n_1 H=3.832...$, $n_2 H=7.016...$, etc. The final result is that for $0\leqslant\zeta<H$, the vorticity generated at the free surface has the form

$$\omega^g(\zeta,\xi,\tau) = -\frac{1}{\sqrt{\tau}}\sum_{k=1}^{\infty}\frac{2}{n_k H J_2(n_k H)}J_1(n_k\zeta) \times\int_0^\infty [R(m,n_k,\tau)\cos(m\xi) + S(m,n_k,\tau)\sin(m\xi)]\,dm, \tag{30a}$$

where

$$R = \exp\left(\frac{\nu m^2}{\tau}\right)\int_{\tau_0}^{\tau}\exp\left(\frac{\nu n_k^2(s^2-\tau^2)}{2}\right) \times\partial_s\left(P(m,s)\exp\left\{-\frac{\nu m^2}{s}\right\}\right)ds - P(m,\tau). \tag{30b}$$

$$S = \exp\left(\frac{\nu m^2}{\tau}\right)\int_{\tau_0}^{\tau}\exp\left(\frac{\nu n_k^2(s^2-\tau^2)}{2}\right) \times\partial_s\left(Q(m,s)\exp\left(-\frac{\nu m^2}{s}\right)\right)ds - Q(m,\tau). \tag{30c}$$

Verifying that $\omega^g(\zeta,\xi,\tau)$ satisfies (26) is delicate. The representation in (29) is discontinuous at $\zeta=H$, and this difficulty also appears in (30). Therefore, one must show that $\omega^g(\zeta,\xi,\tau)$ satisfies (26) in the limit as $\zeta\to H$. To do so, use (30b) and (30c) to replace $R(m,n_k,\tau)$ and $S(m,n_k,\tau)$ in (30a) each by two terms, one integral and one nonintegral. In each case, the exponential factor in the integral terms makes that sum (over $n_k$) well behaved, so that these sums are continuous at $\zeta=H$. Therefore, one can simply evaluate them at $\zeta=H$, where they vanish because $J_1(n_k H)=0$ by (29b). The two sums that remain are discontinuous at $\zeta=H$, but these two sums (over $n_k$) each decouple from the integral (over $m$). For these sums, using (29a) allows one to evaluate the limit ($\zeta\to H$) easily, and to show that $\omega^g(\zeta,\xi,\tau)$ satisfies (26) as $\zeta\to H$.

Verifying that $\omega^g(\zeta,\xi,\tau)$ satisfies (25) for $0<\zeta<H$ is even more delicate, because formal differentiation inside the sum in (30a) leads to divergent series. One way to resolve this difficulty is to show that $\omega^g(\zeta,\xi,\tau)$ is a weak solution of (25). Equivalently, one can establish conventions to *interpret* particular divergent sums. The following conventions arise by formally differentiating (29a) twice:

$$1 = \sum_{k=1}^{\infty}\frac{1}{J_2(n_k H)}J_0(n_k\zeta), \quad 0\leqslant\zeta<H, \tag{31a}$$

$$0=\sum_{k=1}^{\infty}\frac{n_k}{J_2(n_kH)}J_1(n_k\zeta),\quad 0\leqslant\zeta<H. \tag{31b}$$

We reiterate that these are conventions; the sums in (31) may diverge.

By direct calculation from (30),

$$\begin{aligned}\partial_\tau R(m,n_k,\tau)+\nu\left(\tau n_k^2+\frac{m^2}{\tau^2}\right)R&=-\nu\tau n_k^2P(m,\tau),\\ \partial_\tau S(m,n_k,\tau)+\nu\left(\tau n_k^2+\frac{m^2}{\tau^2}\right)S&=-\nu\tau n_k^2Q(m,\tau).\end{aligned} \tag{32}$$

Using (32) and (31b), one can verify by differentiating within the sum and within the integral that $\omega^g(\zeta,\xi,\tau)$ satisfies (25), at least formally. It is evident that $\omega^g(\zeta,\xi,\tau)$ vanishes at $\zeta=0$, and that it is bounded for all $\xi$, for suitable $\{P,Q\}$. This completes the verification that $\omega^g(\zeta,\xi,\tau)$ is a suitable representation of the forced vorticity field.

The corresponding velocity fields are

$$\begin{aligned}u_1^g(\zeta,\xi,\tau)&=\sqrt{\tau}\sum_{k=1}^{\infty}\frac{2}{n_kHJ_2(n_kH)}J_1(n_k\zeta)\\ &\quad\times\int_0^{\infty}\left[\frac{m}{m^2+n_k^2\tau^3}\right][R(m,n_k,\tau)\sin(m\xi)\\ &\quad-S(m,n_k,\tau)\cos(m\xi)]dm,\\ w_1^g(\zeta,\xi,\tau)&=\tau^2\sum_{k=1}^{\infty}\frac{2}{n_kHJ_2(n_kH)}J_0(n_k\zeta)\\ &\quad\times\int_0^{\infty}\left[\frac{n_k}{m^2+n_k^2\tau^3}\right][R(m,n_k,\tau)\cos(m\xi)\\ &\quad+S(m,n_k,\tau)\sin(m\xi)]dm.\end{aligned} \tag{33}$$

For a viscous filament with no initial vorticity, the complete velocity field is the sum of those in (16) and (33).

### C. Conditions at the free surface

One condition at the free surface results from eliminating the pressure between (24c) and (24f), both evaluated at $\zeta=H$:

$$\begin{aligned}\frac{1}{\rho\tau}\partial_\xi p_1&=\nu\tau\left(\partial_\zeta^2w_1+\frac{1}{\zeta}\partial_\zeta w_1\right)+\frac{\nu}{\tau^2}\partial_\xi^2w_1-\frac{1}{\tau}\partial_\tau(\tau w_1),\\ \frac{1}{\rho\tau}\partial_\xi p_1\big|_{\zeta=H}&=\left(\frac{3H}{4\tau^{7/2}}-\frac{\sigma}{\rho H^2}\right)\partial_\xi h_1-\frac{\sigma}{\rho\tau^3}\partial_\xi^3h_1\\ &\quad+\frac{2\nu}{\sqrt{\tau}}\partial_\xi\partial_\zeta u_1\big|_{\zeta=H}.\end{aligned} \tag{34}$$

Two other conditions are shown in (24e) and (24g). These conditions are not independent, because (24e) and (24g) were already used to derive (26). In what follows, we use (34) and (24e), but not (24g).

The next step is to substitute the representations for the velocity fields from (16), and (33), plus the representation for the free surface from (17), into the conditions at $\zeta=H$, in order to obtain evolution equations for the unknown functions $\{A(m,\tau),B(m,\tau),C(m,\tau),D(m,\tau),P(m,\tau),Q(m,\tau)\}$. These equations, along with (28), determine the motion of a viscous liquid filament.

We omit the equations obtained in this way, which are linear but complicated integro-differential equations for the unknown functions listed above. Equations corresponding to these can be found in Ref. 17. In order to simplify the analysis, we now make an additional assumption.

### D. Assumption: The liquid is very viscous

Recall that $R(m,n_k,\tau)$ and $S(m,n_k,\tau)$ are defined in (30). We show in Appendix B that for large viscosity ($\nu\to\infty$) and $\tau>\tau_0$,

$$\begin{aligned}R(m,n_k,\tau)&\to-\frac{n_k^2\tau^3}{m^2+n_k^2\tau^3}P(m,\tau),\\ S(m,n_k,\tau)&\to-\frac{n_k^2\tau^3}{m^2+n_k^2\tau^3}Q(m,\tau).\end{aligned} \tag{35}$$

In terms of the differential equations in (32), (35) asserts that the homogeneous solutions of (32) decay much faster than the time scale on which the forcing terms, $P(m,\tau)$ and $Q(m,\tau)$, evolve. This rapid decay occurs in a very viscous fluid. We now define a ''very viscous fluid'' to be one for which (35) holds.

This assumption simplifies the representation of the velocity field generated by the motion of the free surface, $u_1^g(\zeta,\xi,\tau)$ and $w_1^g(\zeta,\xi,\tau)$. It also reduces the system of linearized equations from third order in time to second order. In terms of $\chi$ from (19) and $(n_kH)$ from (29b), define

$$\vartheta(\chi):=2\sum_{k=1}^{\infty}\frac{\chi^2}{\chi^2+(n_kH)^2}. \tag{36}$$

In addition, recall one more identity (Ref. 23, p. 361):

$$J_0(n_kH)+J_2(n_kH)=0.$$

Using all of these plus (35) in (33) leads to limiting values (as $\zeta\to H$) of the quantities that appear in the boundary conditions at the free surface:

$$\begin{aligned}u_1^g(\zeta,\xi,\tau)&\to0,\\ w_1^g(\zeta,\xi,\tau)&\to\frac{H}{\tau}\int_0^{\infty}\frac{\vartheta'(\chi)}{2\chi}[P(m,\tau)\cos(m\xi)\\ &\quad+Q(m,\tau)\sin(m\xi)]dm,\\ \partial_\zeta\partial_\xi u_1^g(\zeta,\xi,\tau)&\to\frac{\sqrt{\tau}}{2H}\int_0^{\infty}\chi\vartheta'(\chi)[P(m,\tau)\cos(m\xi)\\ &\quad+Q(m,\tau)\sin(m\xi)]dm,\\ \nu\tau\left(\partial_\zeta^2w_1^g+\frac{1}{\zeta}\partial_\zeta w_1^g\right)&+\frac{\nu}{\tau^2}\partial_\xi^2w_1^g\\ &\to\frac{\nu}{H}\int_0^{\infty}[2+\vartheta(\chi)][P(m,\tau)\cos(m\xi)\\ &\quad+Q(m,\tau)\sin(m\xi)]dm.\end{aligned} \tag{37}$$

The last of these makes use of the (counterintuitive) limit of (31a) as $\zeta \to H$.

### E. Linear stability

Finally, substitute [(16), (17), and (37)] into (34) and into (24e). The result is two identical sets of ordinary differential equations, one for $\{(B(m,\tau),C(m,\tau),P(m,\tau)\}$, and the other for $\{(A(m,\tau),D(m,\tau),-Q(m,\tau)\}$. The first set is

$$\begin{aligned}\frac{\nu}{H}(2+\vartheta(\chi))P-\frac{H}{\tau}\partial_\tau\left(\frac{\vartheta'(\chi)}{2\chi}P\right)-\frac{1}{\tau}\partial_\tau(\tau I_0(\chi)B)\\ =\left(\frac{3}{4\tau^{5/2}}-\frac{\sigma\tau}{\rho H^3}(1-\chi^2)\right)\chi C+\frac{\nu}{H}\chi\vartheta'(\chi)P\\ +\frac{2\nu\tau}{H^2}\chi^2 I_1'(\chi)B,\\ \partial_\tau C=\sqrt{\tau}I_1(\chi)B.\end{aligned} \tag{38}$$

This set of equations, along with (28), determine the linearized stability of a very viscous filament. To analyze this system, it is convenient to rewrite it as a second-order differential equation for $C(m,\tau)$. In addition, we eliminate $\vartheta(\chi)$ by using an identity derived in Appendix C:

$$\vartheta(\chi)=\chi\frac{I_0(\chi)}{I_1(\chi)}-2. \tag{39}$$

The final result, after some algebra, is

$$\alpha\frac{\partial^2 C}{\partial\tau^2}+\frac{\beta}{\tau}\frac{\partial C}{\partial\tau}-\frac{\Gamma}{\tau^2}C=0, \tag{40}$$

where $\chi$ is defined in (19), and

$$\alpha(\chi)=\left(\frac{\chi I_0(\chi)}{I_1(\chi)}\right)^2-\left(\frac{\chi I_0(\chi)}{I_1(\chi)}\right)-\chi^2, \tag{41a}$$

$$\begin{aligned}\beta\left(\chi,\frac{\nu m^2}{\tau}\right)=3\left(\frac{\chi I_0(\chi)}{I_1(\chi)}\right)^3-7\left(\frac{\chi I_0(\chi)}{I_1(\chi)}\right)^2+4\left(\frac{\chi I_0(\chi)}{I_1(\chi)}\right)\\ -3\chi^2\left(\frac{\chi I_0(\chi)}{I_1(\chi)}\right)+4\chi^2+\left(\frac{2\nu m^2}{\tau}\right)\\ \times\left[\left(\frac{\chi I_0(\chi)}{I_1(\chi)}\right)^2-\chi^2-1\right],\end{aligned} \tag{41b}$$

$$\begin{aligned}\Gamma\left(\chi,\frac{\sigma m^2\sqrt{\tau}}{\rho H},\frac{\nu m^2}{\tau}\right)=\frac{\sigma m^2\sqrt{\tau}}{\rho H}(1-\chi^2)+\frac{3\nu m^2}{\tau}\alpha(\chi)\\ +\frac{3}{4}\left[6\left(\frac{\chi I_0(\chi)}{I_1(\chi)}\right)^3\right.\\ -16\left(\frac{\chi I_0(\chi)}{I_1(\chi)}\right)^2+8\left(\frac{\chi I_0(\chi)}{I_1(\chi)}\right)\\ \left.-6\chi^2\left(\frac{\chi I_0(\chi)}{I_1(\chi)}\right)+9\chi^2\right].\end{aligned} \tag{41c}$$

A filament of a very viscous liquid is unstable if (40) has any solutions that grow in time.

Alternatively, we may write (40) in Sturm–Liouville form:

$$\frac{\partial}{\partial\tau}\left[\tau\Delta\frac{\partial C}{\partial\tau}\right]-\frac{\Delta\Gamma}{\alpha\tau}C=0, \tag{42}$$

where

$$\Delta\left(\chi,\frac{\nu m^2}{\tau},\tau\right)=\exp\left(\int^\tau\left(\frac{\beta-\alpha}{\alpha\tau}\right)d\tau\right).$$

Observe that $\Delta$ is exponential with a real-valued exponent, so $\Delta>0$, and (42) is indeed in Sturm–Liouville form. In Appendix D, we show that $\alpha(\chi)>0$ for $\chi\geqslant 0$. Therefore (42), and (40), have a nonoscillatory growing solution, and the filament is unstable, if

$$\Gamma\left(\chi,\frac{\sigma m^2\sqrt{\tau}}{\rho H},\frac{\nu m^2}{\tau}\right)>0, \tag{43}$$

where $\Gamma$ is given in (41c). This is the criterion for unstable wave numbers for a very viscous filament; it is one of the two main results in this section.

For which dimensionless wave numbers ($\chi$) is $\Gamma>0$? In (41c), the first term on the right-hand side represents the effect of surface tension; it is positive for $0<\chi<1$. The second term represents the effect of viscosity; because $\alpha(\chi)>0$ for all $\chi>0$, this term is always positive. We show in Appendix D that the last term in (41c) is positive for $0<\chi<\mathbf{X}$ ($\mathbf{X}\approx 2$). Thus, every filament is unstable in a very viscous liquid, because the set of unstable wave numbers always includes $0<\chi<1$, and it may include more.

### F. Growth rates of unstable modes

To compute actual rates of growth of unstable modes, one must integrate (40) or (42). To aid in that integration, we show in Appendix D that

$$\alpha(\chi)>0 \quad \text{for } \chi>0, \tag{44a}$$

$$\alpha(\chi)\to 2 \quad \text{as } \chi\to 0, \tag{44b}$$

$$\beta\left(\chi,\frac{\nu m^2}{\tau}\right)-\alpha(\chi)>0 \quad \text{for } \chi>0, \quad \frac{\nu m^2}{\tau}\geqslant 0, \tag{44c}$$

$$\beta\left(\chi,\frac{\nu m^2}{\tau}\right)-\alpha(\chi)\to 2 \quad \text{as } \chi\to 0, \quad m\to 0. \tag{44d}$$

In addition, recall that (40) or (42) applies only for a very viscous liquid. For wave number $m>0$, the viscosity ($\nu$) of the liquid appears in both $\beta$ and $\Gamma$, so each of these coefficients is asymptotically large. We show next that in the ''very viscous'' limit, (40) approximately splits into two first-order equations, which we solve approximately. Let $\mu\gg 1$ denote a large dimensionless parameter representing the viscosity of the filament, e.g., $\mu=\nu m^2/\tau$. For a very viscous liquid and $m>0$, it follows from (41) that

$$\alpha=O(1), \quad \beta=O(\mu), \quad \Gamma=O(\mu). \tag{45}$$

Then (40) has a fast-changing solution, $C_f(m,\tau)$, with

$$C_f=O(1), \quad \frac{\partial C_f}{\partial\tau}=O(\mu), \quad \frac{\partial^2 C_f}{\partial\tau^2}=O(\mu^2).$$

For this solution, (40) becomes approximately

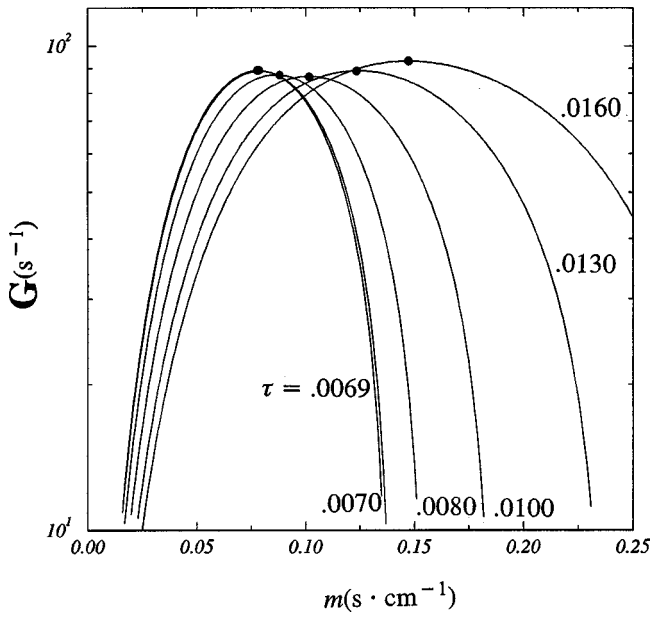


FIG. 3. The instantaneous growth rate for unstable modes for fluid A1, from Eq. (48), The growth rate ($G$) is plotted as a function of wave number ($m$) for various times during the interval in which $dh/dz=0$. A dot (●) marks the most unstable mode at each time.

$$\alpha\frac{\partial^2 C_f}{\partial\tau^2}+\frac{\beta}{\tau}\frac{\partial C_f}{\partial\tau}\sim 0,$$

so that

$$C_f(m,\tau)\sim C_f(m,\tau_0)\exp\left(-\int_{\tau_0}^{\tau}\frac{\beta}{\alpha\tau}d\tau\right). \tag{46}$$

From (44), $\{\beta/\alpha\tau\}>1$, so this solution decays, relatively fast.

The other solution of (40), $C_s(m,\tau)$, changes slowly:

$$C_s=O(1),\quad \frac{\partial C_s}{\partial\tau}=O(1),\quad \frac{\partial^2 C_s}{\partial\tau^2}=O(1).$$

For this solution, (40) becomes approximately

$$\frac{\beta}{\tau}\frac{\partial C_s}{\partial\tau}-\frac{\Gamma}{\tau^2}C_s\sim 0,$$

so that

$$C_s(m,\tau)\sim C_s(m,\tau_0)\exp\left(\int_{\tau_0}^{\tau}\frac{\Gamma}{\beta\tau}d\tau\right). \tag{47}$$

If (43) holds for a particular $m>0$, then $C_s(m,\tau)$ grows with $\tau$, relatively slowly. This is the unstable mode for this $m$.

Both $\beta$ and $\Gamma$ depend on $\tau$, so the unstable modes do not exhibit simple exponential growth. The instantaneous growth rate of an unstable mode is given by

$$G=\frac{\Gamma}{\beta\tau}, \tag{48}$$

and it changes with time. Moreover, the ''most unstable wave number'' [i.e., the wave number $m$ that maximizes the growth rate in (48) at fixed $\tau$], changes with time; this is another difference between a falling liquid filament and a uniform jet. Figure 3 shows graphs of instantaneous growth rate ($G$) vs wave number ($m$), plotted at various times, using the parameters that correspond to the experiment in Fig. 1. Please note the following points.

(1) At each time, there is a most unstable wave number ($m$), shown with a dot (●) in Fig. 3. As time increases, this maximal wave number increases, even over the fraction of a second during which the filament survives.

(2) The ''wave number'' $m$ has dimensions of (time/length) instead of (1/length). The corresponding wavelength is given by $\lambda=2\pi\tau/m$. Therefore, if the maximal $m$ remains constant in time, its corresponding wavelength grows (linearly) in time. If the maximal $m$ grows slower than linearly, then the most unstable wavelength also changes in time. Typically, the instability of a falling liquid filament does *not* generate disturbances of constant wavelength.

(3) Some of the curves in Fig. 3 have rather broad maxima, so near each maximal wave number is a range of other wave numbers with growth rates nearly as large as the maximal value. In an experiment, therefore, this instability is likely to select a band of nearly maximal wave numbers, instead of just one.

(4) The band of wave numbers with instantaneous growth rates near the maximum becomes more broad as time increases. The value of the maximal growth rate itself does not change significantly with time.

To summarize this section, the linearized stability of a very viscous liquid filament is now completely explicit. Here are the main results. The set of unstable wave numbers is defined by (43). For each unstable wave number, the growth of the unstable mode is approximately given by (47). For a given filament, a graph like that in Fig. 3 shows which wave numbers grow most rapidly, and how their instantaneous growth rates change with time. A particular liquid filament qualifies as ''very viscous'' if the time scale of growth in (47) is slow in comparison with the time scale of decay in (32).

In Sec. V, we use these results to predict whether a given liquid filament pinches off first near its ends, like the filament in Fig. 1, or if it pinches off in its interior.

## V. WHERE DOES A FILAMENT PINCH OFF?

The filament in Fig. 1 pinches off near its ends (first at the bottom of the filament, then at the top). This behavior is commonly observed in experiments.[2–5,11] It is called ''end-pinching'' in Ref. 11, and it occurs in filaments that form either because of gravity, as in our Fig. 1 and in Refs. 2–5 or without gravity.[11] However, not all filaments pinch off first near their ends, as noted in Ref. 11 for filaments and drops created without gravity in a four-roll mill. Figure 4 shows the results of an experiment like that in Fig. 1, but for a more viscous fluid. (This experiment uses fluid E, described in Table I.) Several differences appear in the motion of these two filaments.

(1) More viscous filaments survive longer. (This can already be inferred from Fig. 2.) As a result, the experiment in Fig. 4 lasts longer than that in Fig. 1.

(2) Because it lasts longer (in time), the filament in Fig. 4 grows to a much longer length than that in Fig. 1. As a

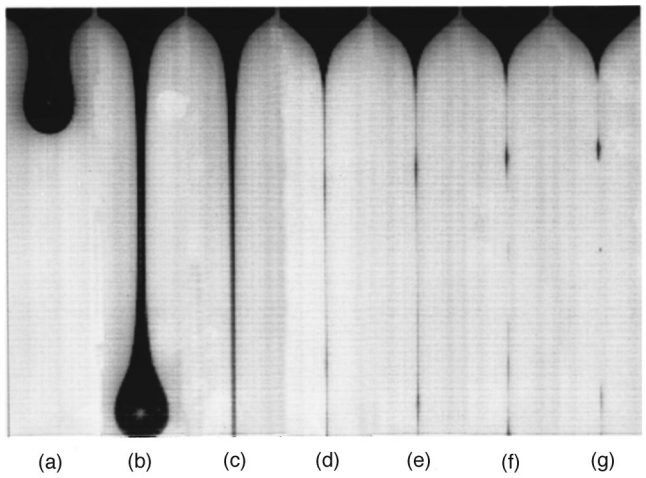


FIG. 4. Images of the drop and filament for fluid E, using a spatial resolution of 95.5 $\mu$m/pixel and a temporal resolution is 4000 fps. Image size is $0.45\times2.27$ cm$^2$. Times of images (referenced to times shown in Figs. 2 and 5) are (a) $-0.1072$ s; (b) $-0.0107$ s; (c) 0.0216 s; (d) 0.0883 s; (e) 0.0933 s; (f) 0.0966 s; (g) 0.0980 s.

result, we are unable to show the entire filament in Fig. 4, except during the first two frames.

(3) The primary filament in Fig. 1 maintains a relatively uniform radius (so $dh/dz\approx0$) while its ends neck down and then pinch off. By comparison, Fig. 4(d) shows that in this experiment the primary filament exhibits spatial variations (so $dh/dz\neq0$) while the end of the filament near the orifice (i.e., at the top of the figure) does not change its shape appreciably. Similarly, we observed no necking down of the filament at its drop-end (although this cannot be confirmed from Fig. 4).

(4) A significant difference between the filaments in Figs. 1 and 4 is that the filament in Fig. 4 pinches off at several points interior to the filament, whereas the filament in Fig. 1 pinches off near its ends. The objective of this final section is to provide a criterion to predict which of these possibilities will occur for a given filament.

All of the fluids depicted in Fig. 2 are ''very viscous,'' according to (35). Thus using the analysis of Sec. IV, we now propose a criterion to determine whether a given filament pinches off near its ends or at interior points. As an example, consider the filament in Fig. 1. For this filament, Fig. 3 shows the instantaneous growth rates of disturbances of various wave numbers. However, Fig. 3 is based on the simplifying assumption that the filament is infinitely long. For a filament of finite length, like that shown in Fig. 1, only some of these wave numbers are allowed, because only some of them correspond to wavelengths that fit into the finite length of the filament. Here is our criterion.

*For a given filament, if the most unstable wave mode has the longest wavelength that fits into the finite length of the filament, then that filament pinches off first near its ends. If the most unstable wave mode has a wavelength that is shorter than the length of the filament, then the filament pinches off at one or more interior points.*

Below are some comments and disclaimers that are required in using this criterion, followed by a detailed outline of how it applies for the eight experiments shown in Fig. 2.

(1) We assume here that there is no external forcing, which can artificially excite a wave mode other than the most unstable mode.

(2) For a falling liquid filament, both the length of the filament and the wavelength of a given mode change with time. Therefore, some work is required to determine whether the (changing) wavelength of a particular mode fits into the (changing) length of the filament. That determination is made explicit in the outline that follows.

(3) We apply this criterion only at early times. The linearized stability analysis in Sec. IV is valid only for small disturbances, so its validity ceases well before the filament actually pinches off.

(4) In practice, as described in the following, we apply the criterion only over the time interval that begins when the primary filament first forms (i.e., when a region forms with $\partial h/\partial z=0$), and ends when we observe significant spatial variations on the primary filament (i.e., when $\partial h/\partial z\neq0$). This is the same time interval used for Fig. 2.

Figure 5 shows how the criterion applies for the eight experiments discussed in Fig. 2.

(a) For each experiment, we find the most unstable wave number, $m$, at the initial time ($t=0$, when $\tau=t^*$). The corresponding wavelength is $\lambda=2\pi\tau/m=2\pi t^*/m$. This is the most unstable wavelength, initially. If this wavelength exceeds the measured length of the primary filament at $\tau=t^*$, then we choose the wavelength equal to the filament length, and find the corresponding value of $m$. (These values of $m$ are listed in Table III, in Appendix A.) The shape of the curves in Fig. 3 guarantees that this is the most unstable wave number for a filament of this length.

(b) Holding $m$ constant, the wavelength of this mode grows linearly in time, according to $\lambda=2\pi\tau/m$. Each solid line in Fig. 5 represents the (changing) wavelength of the mode that was the most unstable mode that fit into the filament at $t=0$.

(c) Also shown in Fig. 5 are the lengths of the primary filament, measured during the interval in which $\partial h/\partial z=0$ for that experiment. These time intervals differed for different experiments, as Fig. 5 shows.

(d) For the first six experiments shown in Fig. 5 [i.e., 5(a)–5(f), corresponding to fluids A1, A2, B1, B2, B3, C], the wavelength of the (initially) most unstable mode either exceeds or equals the length of the primary filament during the relevant time interval. According to the above-given criterion, these filaments should pinch off at their ends first, and they did. For each of the last two experiments [i.e., Figs. 5(g) and 5(h), corresponding to fluids D and E], the most unstable wavelength fit inside the length of the primary filament. The above-mentioned criterion predicts that these two filaments should pinch off at points internal to the filament (instead of near the ends), and they did.

(e) The filaments of fluids A, B, and C all pinched off first near their ends, as predicted. The contracting filaments of A1, A2, B1, and B2 remained stable after pinch-off and each resulted in one satellite drop. The contracting filament of fluid B3 showed some nonuniformity, but the nascent instability did not grow, and one satellite drop was formed.

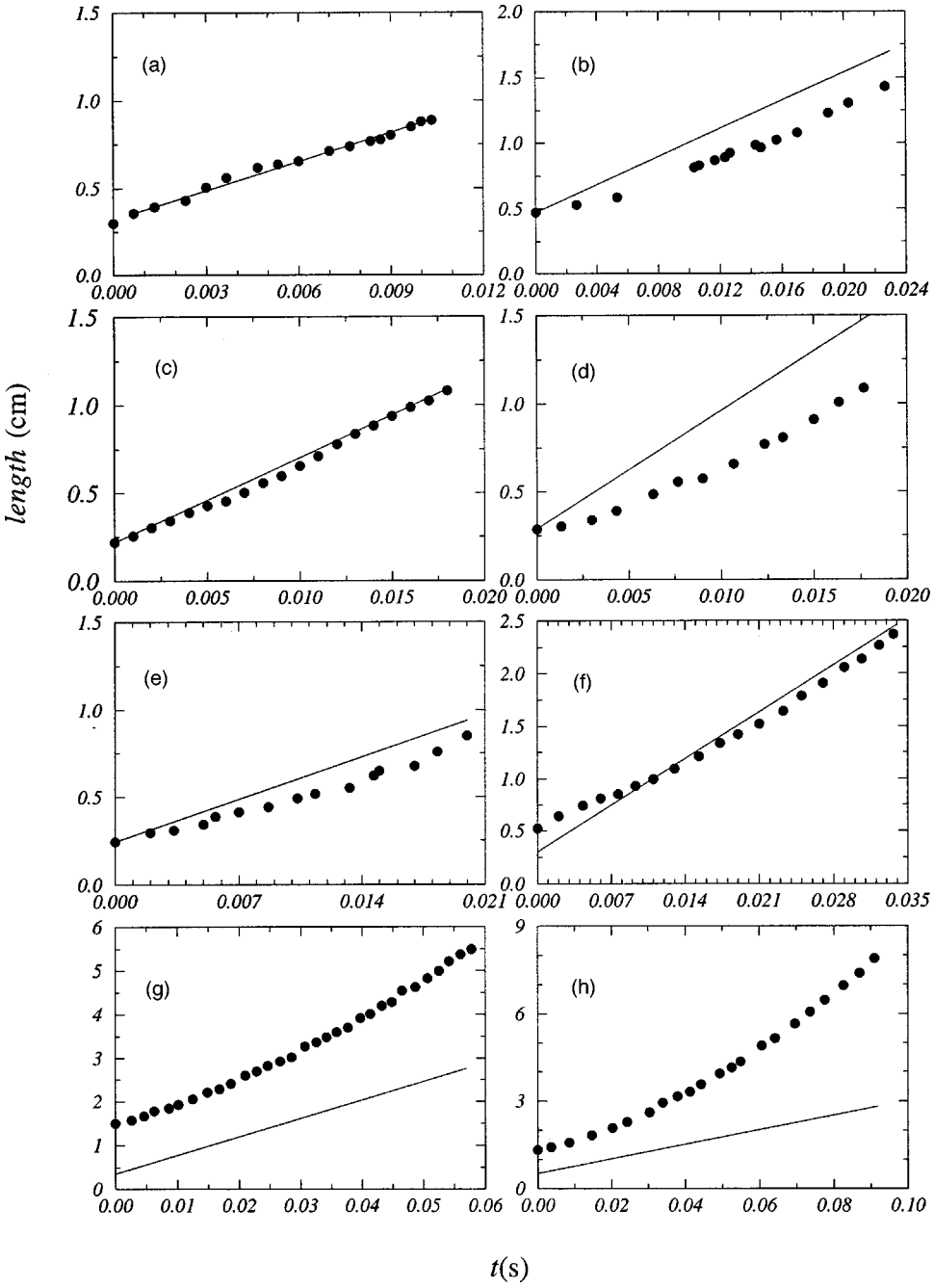


FIG. 5. Filament length vs time for the eight experiments of Fig. 2, listed in Table I. Circles denote measurements of filament length. Lines denote the changing wavelength of the mode that was most unstable and that fit into the filament length at $t=0$. (a) Fluid A1; (b) fluid A2; (c) fluid B1; (d) fluid B2; (e) fluid B3; (f) fluid C; (g) fluid D; (h) fluid E.

The contracting filament of fluid C exhibited instabilities that grew substantially, causing the filament to break up into several satellite drops.

For all of our experimental data, therefore, this criterion successfully predicts whether a filament pinches off first near its ends or at internal points. To our knowledge, this is the first theoretical prediction of this behavior.

## ACKNOWLEDGMENTS

We thank Bernard Deconinck for discovering (39), James Meiss for catching a logical error in an early version of this paper, Joe Hammack for many helpful discussions, and an anonymous referee for bringing Refs. 16 and 17 to our attention. H. S. acknowledges the kind hospitality of the Physics Department, University of Tokyo, where this work was initiated, and of the Mathematics Department, Hong Kong University of Science and Technology, where it was completed. His work in Japan was supported by the Japan Society for the Promotion of Science. The work was also supported in part by NSF Grant Nos. DMS-9304390 and DMS-9731097. The experiments were supported by fellowships from the David & Lucile Packard Foundation and the Alfred P. Sloan Foundation, and from NSF Grant No. DMS-9257456.

## APPENDIX A: EXPERIMENTAL APPARATUS, MATERIALS, AND PROCEDURES

The experimental apparatus comprised silicone and commercial vegetable oils, Lucite reservoirs, and an imaging sys-

TABLE II. Spatial and temporal resolution for each experiment shown in Fig. 2.

| Fluid | Spatial resolution ($\mu$m pixel) | Temporal resolution (frame/s) |
|---|---|---|
| A1 | 110 | 3000 |
| A2 | 111 | 3000 |
| B1 | 33.6 | 3000 |
| B2 | 25.6 | 3000 |
| B3 | 33.6 | 3000 |
| C | 39.6 | 6000 |
| D | 63.7 | 3000 |
| E | 42.1 | 3000 |

tem. Table I lists the fluid properties (viscosity, surface tension, density) as well as the experimental parameters (flow rate and orifice size).

Fluids B, C, D, and E were silicone oils (Dow Corning) chosen for their ranges of viscosities from about 100 to 1000 times more viscous than water. The surface tension of these oils did not vary significantly. Fluid A was a commercial vegetable oil (Weis brand), with a surface tension that varied significantly from that of the silicone oils. Viscosities were measured in a temperature-controlled bath; see Ref. 5 for details of fluids A and B. Surface tension was measured with a DuNouy tensiometer at room temperature. Experiments A1 and A2 used the same fluid with different flow rates. Experiments B1–B3 used the same fluid with different orifice sizes. The flow rates were measured as an average over several drops.

For a given experiment, the oil was poured into a reservoir and left open to the atmosphere. It dripped from an orifice under gravity at a rate controlled by a needle valve. The orifice was machined to have a flat edge so that the oil coated the surface area between the inner and outer edges. The radius of the outer edge is listed in Table I. The dimensions of the overall apparatus are given in Ref. 5. The apparatus was enclosed in a plastic box that was not temperature controlled but stopped air-currents and external contamination.

A Kodak EktaPro 1012 EM Motion Analyzer captured images of the falling drop with spatial and temporal resolutions listed in Table II.

Illumination was obtained using silhouette photography, following Ref. 24, with a 600 W lamp, an experimental grade one-way transparent mirror (Edmund Scientific, A40,047) and reflective screen material (Scotchlite 3M 7615). The mirror, placed between the camera and drop, was oriented at a 45° angle to the camera's face. Approximately 50% of the incident light was reflected toward the drop. The reflective material, placed directly behind the drop, reflected the incoming light rays back toward the drop. The effect of this setup was to render the drop as a shadow. The reflective material, rated as 98% efficient, sends back the light within an angle of 0.5° of its initial path,[24] resulting in less scattering of light around the edges of the imaged drops and a higher-contrast image.

Images were visible on a monitor and down-loaded to video, to hard copy, and/or to a computer. Measurements of filament widths and filament lengths were obtained directly from the monitor, from the hard copies and/or using PhotoAdobe on the computer for image enhancement and edge detection. Comparisons among the different techniques did not show significant variability.

Measurements for filament width and length were obtained as follows. First, for all fluids, the experiment was imaged with a coarse resolution so that the entire drop was visible until pinch-off. From this global view, reference points were obtained. In particular, we noted the location of the drop when we first judged a filament with $\partial h/\partial z=0$ to have formed. Then we noted the interval of time that passed while the drop fell from this location until we first observed either necking at the ends of the filament (for fluids A, B, and C or wavelike instabilities on the filament (for fluids D and E). Measurements of filament width for fluid A were obtained from this global view during this time-interval.

Second, measurements of length were obtained from this time series by placing the reticule from the imager onto the filament boundary and measuring the length under it for which $\partial h/\partial z=0$. These measurements are accurate to within $\pm 0.01$ cm.

Third, we zoomed-in the imager to obtain higher-resolution for measurements of filament width, for all fluids except C. The resolutions are listed in Table II. In these images a portion of the filament was in the image, but neither the orifice nor the drop was in the image during measurements. The position of the image was known relative to the orifice and to the reference location obtained from the global view. We waited a known (small) amount of time after the drop passed this location. Then this time was defined to be $t=0$ in the corresponding measurements of filament width. (Filament lengths are also referenced to this time.) Measurements were taken during the time interval over which $dh/dz=0$, determined from the global view.

To obtain values of $H$ and $t^*$ from the measurements of filament width, we calculated $(H,t^*)$ from every possible combination of two data points. Then we considered the error (in a least-squares sense) between the calculated values of $H$ and the corresponding values of $h\sqrt{\tau}$. We considered the values of $(H,t^*)$ that provided the smallest error, the values obtained as an average over some small error, and in the end, we chose the values that, by eye, showed the best agreement with the entire set of data points. These values of $H$ correspond to the horizontal lines in Fig. 2 and are listed along with $t^*$ in Table III. They could have changed by about $\pm 5\%$ each. This variation did not effect the results of the stability calculations. The results of these calculations are also listed in Table III. In particular, we list the values of the wave number, $m$, that had the maximum growth rate [from Eq. (48)] at time $t=0$. For fluids (A, B), this occurred at the longest wavelength that fit into the filament at that time; for fluids (C, D, E), it occurred at the peak of the curve corresponding to that shown in Fig. 3.

Finally, here are two comments about our observations. First, because of inadequate spatial and temporal resolution, we were unable to measure modal amplitudes as a function of time. Instead, we measured wavelengths that were observable at various times and at various spatial resolutions. We

TABLE III. Measured values of $\{H,t^*\}$ and corresponding calculations of the most unstable wave number $m$ at $\tau=t^*$.

| Fluid | $H$ [cm*(s)$^{1/2}$] | $t^*$ (s) | $m(t=0)$ (s/cm) |
|---|---|---|---|
| A1 | 0.0058 | 0.0069 | 0.124 |
| A2 | 0.0061 | 0.0089 | 0.118 |
| B1 | 0.0018 | 0.0045 | 0.130 |
| B2 | 0.0021 | 0.0043 | 0.094 |
| B3 | 0.0025 | 0.0070 | 0.180 |
| C | 0.0020 | 0.0048 | 0.099 |
| D | 0.0019 | 0.0083 | 0.148 |
| E | 0.0028 | 0.0211 | 0.253 |

found that when we observed the filaments with a coarse resolution, we could not resolve the short wavelengths; when we observed with a fine resolution, we could not resolve the long wavelengths. For example, when viewing experiment E at $\tau=0.17$ s, with a fine resolution that allowed only a portion of the filament into the image, we observed wavelengths of about 0.6 cm. The image size was such that we could not also observe wavelengths larger than about 1 cm. The amplitudes were essentially 1 pixel. Thus, when viewing the filament at a coarser resolution, we could not resolve these amplitudes and would not observe those modes. Instead, when viewing the filament at a coarse resolution that allowed the whole filament-drop combination into the image, we observed waves with lengths of about 3 cm. They also had amplitudes of about 1 pixel. (We note that the most unstable wavelength at $t=t^*$ gives a wavelength at $\tau=0.17$ of 4.2 cm.) Presumably, fluids such as D and E, for which pinch-off occurs within the filament, admit many unstable modes and at present we cannot observe their evolutions.

Second, we also note that previous work[2,5] showed that pinch-off occurred in a secondary filament localized at the end of the filament near the drop. Reference 2 observed this same structure at the orifice, while Ref. 5 did not observe it for fluid B2. It was conjectured in Ref. 5 that this difference was due to the difference in orifice sizes, since that of Ref. 2 was significantly larger than that in Ref. 5. Our observations support this conjecture: when we used the same fluid with a larger orifice (in experiment B3), the secondary filament did form.

## APPENDIX B: LIMITING BEHAVIOR OF $R(m,n_k,\tau)$

$R(m,n_k,\tau)$ and $S(m,n_k,\tau)$ are defined in (30). In this appendix we show that $R(m,n_k,\tau)$ satisfies (35) for large viscosity ($\nu\to\infty$), and that $R(m,n_k,\tau)\to 0$ for small viscosity ($\nu\to 0$). The behavior of $S(m,n_k,\tau)$ is similar. In what follows, we assume that both $P(m,\tau)$ and $\partial_\tau P(m,\tau)$ have bounds that are independent of $\nu$.

Define

$$\phi(s)=-\nu n_k^2(\tau^2-s^2)/2+\nu m^2(\tau^{-1}-s^{-1}).$$

so that

$$\partial_s\phi=\nu\left[n_k^2 s+\frac{m^2}{s^2}\right]>0 \quad \text{for } 0<s<\infty,$$

and

$$\phi(\tau)=0 \quad \text{at } s=\tau.$$

Then (30b) can be written as

$$\begin{aligned}R(m,n_k,\tau)&=\int_{\tau_0}^{\tau}e^{\phi(s)}\partial_s P(m,s)ds\\&\quad+\int_{\tau_0}^{\tau}e^{\phi(s)}\frac{\nu m^2}{s^2}P(m,s)ds-P(m,\tau),\\&=R1+R2-P.\end{aligned}$$

But

$$\begin{aligned}R_2&=\int_{\tau_0}^{\tau}e^{\phi(s)}\partial_s\phi\left(\frac{m^2/s^2}{n_k^2 s+m^2/s^2}\right)P(m,s)ds\\&=e^{\phi(s)}\left(\frac{m^2/s^2}{n_k^2 s+m^2/s^2}\right)P(m,s)\Big|_{\tau_0}^{\tau}\\&\quad-\int_{\tau_0}^{\tau}e^{\phi(s)}\partial_s\left[\frac{m^2/s^2}{n_k^2 s+m^2/s^2}P(m,s)\right]ds,\\&=\left(\frac{m^2}{n_k^2\tau^3+m^2}\right)P(m,\tau)\\&\quad-\int_{\tau_0}^{\tau}e^{\phi(s)}\partial_s\left[\frac{m^2/s^2}{n_k^2 s+m^2/s^2}P(m,s)\right]ds,\end{aligned}$$

where we have used $P(m,\tau_0)=0$ and $\phi(\tau)=0$. Therefore,

$$\begin{aligned}R(m,n_k,\tau)&=-\left(\frac{n_k^2\tau^3}{n_k^2\tau^3+m^2}\right)P(m,\tau)\\&\quad+\int_{\tau_0}^{\tau}e^{\phi(s)}\partial_s\left[\frac{n_k^2 s}{n_k^2 s+m^2/s^2}P(m,s)\right]ds.\end{aligned}$$

In the last integral, both the quantity in square brackets and its derivative have bounds that are independent of $\nu$, so the integral vanishes as $\nu\to\infty$ by Watson's Lemma.[25] This leads to (35).

To evaluate $R(m,n_k,\tau)$ as $\nu\to 0$, expand $\phi(s)$ in a Taylor series in powers of $\nu$, and integrate term by term. The first integral cancels $(-P(m,t))$, and the other integrals vanish as $\nu\to 0$. Because $R(m,n_k,\tau)$ and $S(m,n_k,\tau)$ both vanish as $\nu\to 0$, one can show that the theory for a viscous fluid reproduces that of an inviscid fluid as $\nu\to 0$.

## APPENDIX C: BOUNDS ON $\vartheta(\chi)$ and on $I_0(\chi)/I_1(\chi)$

*Lemma 1:* With $\vartheta(\chi)$ defined in (36),

$$\vartheta(0)=0, \quad \vartheta'(0)=0,$$

$$\vartheta(\chi)>0 \quad \text{if } \chi>0, \quad \vartheta'(\chi)>0 \quad \text{if } \chi>0;$$

$$\vartheta(\chi)<\chi \quad \text{if } \chi>0.$$

*Proof:* It follows from (36) that

$$\vartheta'(\chi)=4\chi\sum_{k=1}^{\infty}\frac{(n_k H)^2}{[\chi^2+(n_k H)^2]^2}. \tag{C1}$$

For $k \geqslant 1$, $k\pi < n_k H$. Therefore the series for $\vartheta(\chi)$ converges, as does that for $\vartheta'(\chi)$. Then it follows from their series that $\vartheta(0)=0=\vartheta'(0)$, and that $\vartheta(\chi)>0$, $\Theta'(\chi)>0$ for $\chi>0$. To establish an upper bound on $\vartheta(\chi)$ for $\chi>0$, observe that

$$\vartheta(\chi)=2\chi^2\sum_{k=1}^{\infty}\frac{1}{\chi^2+(n_kH)^2}<2\chi^2\sum_{k=1}^{\infty}\frac{1}{\chi^2+(k\pi)^2},$$

so

$$\vartheta(\chi)<2\chi^2\int_0^{\infty}\frac{dk}{\chi^2+(k\pi)^2}=\frac{2\chi}{\pi}\int_0^{\infty}\frac{dy}{1+y^2}=\chi.$$

*Remark:* Lemma 2 is due to Bernard Deconinck.

*Lemma 2:*

$$\vartheta(\chi)=\chi\frac{I_0(\chi)}{I_1(\chi)}-2.$$

*Proof:* The Bessel function $J_1(Y)$ can be written in terms of an infinite product:[26]

$$J_1(Y)=\frac{Y}{2}\prod_{k=1}^{\infty}\left(1-\frac{Y^2}{(n_kH)^2}\right),$$

where $J_1(n_kH)=0$. Taking logarithms and differentiating yields

$$\ln J_1(Y)=\ln Y-\ln 2+\sum_{k=1}^{\infty}\ln\left(1-\frac{Y^2}{(n_kH)^2}\right),$$

so

$$\frac{J_1'(Y)}{J_1(Y)}=\frac{1}{Y}-\sum_{k=1}^{\infty}\frac{2Y/(n_kH)^2}{1-Y^2/(n_kH)^2}$$

$$=\frac{1}{Y}-\frac{2}{Y}\sum_{k=1}^{\infty}\frac{Y^2}{(n_kH)^2-Y^2}. \tag{C2}$$

But $I_1(\chi)=-iJ_1(i\chi)$ for $\chi \geqslant 0$ (Ref. 23, p. 375). Set $Y=i\chi$ in (C2):

$$\frac{I_1'(\chi)}{I_1(\chi)}=\frac{1}{\chi}+\frac{2}{\chi}\sum_{k=1}^{\infty}\frac{\chi^2}{(n_kH)^2+\chi^2}=\frac{1}{\chi}+\frac{\vartheta(\chi)}{\chi}. \tag{C3}$$

From Ref. 22,

$$\frac{d}{d\chi}[\chi I_1(\chi)]=\chi I_0(\chi),\quad \frac{d}{d\chi}I_0(\chi)=I_1(\chi), \tag{C4}$$

Therefore $I_1'(\chi)/I_1(\chi)=I_0(\chi)/I_1(\chi)-1/\chi$. Substituting this into (C3) yields Lemma 2.

*Lemma 3:* $I_0(\chi)/I_1(\chi)$ has the following properties.

(i) $$\frac{I_0(\chi)}{I_1(\chi)}=\frac{2}{\chi}\left[1+\frac{1}{2}\left(\frac{\chi}{2}\right)^2-\frac{1}{12}\left(\frac{\chi}{2}\right)^4+O(\chi^6)\right]$$

as $\chi\to 0$,

(ii) $$\frac{I_0(\chi)}{I_1(\chi)}=1+\frac{1}{2\chi}+\frac{3}{2}\left(\frac{1}{2\chi}\right)^2+O(\chi^{-3})]$$

as $\chi\to\infty$,

(iii) $$\frac{d}{d\chi}\left(\frac{I_0}{I_1}\right)=1-\left(\frac{I_0}{I_1}\right)^2+\frac{1}{\chi}\left(\frac{I_0}{I_1}\right)\quad \text{for } 0<\chi<\infty.$$

*Proof:* Both $I_0(\chi)$ and $I_1(\chi)$ have convergent Taylor series expansions near $\chi=0$.[22,23] The representation in (i) follows from these. Similarly, both functions have asymptotic expansions as $\chi\to\infty$, and (ii) follows from these. The differential equation in (iii) follows from those in (C4).

*Lemma 4:*

$$\frac{I_0(\chi)}{I_1(\chi)}>\frac{1}{2\chi}+\sqrt{\frac{1}{(2\chi)^2}+1}\quad \text{for } 0<\chi<\infty.$$

*Proof:* Define

$$y(\chi):=\frac{1}{2\chi}+\sqrt{\frac{1}{(2\chi)^2}+1},$$

so

$$1-y^2+\frac{y}{\chi}=0. \tag{C5}$$

Lemma 4 asserts that $I_0(\chi)/I_1(\chi)>y(\chi)$ for $0<\chi<\infty$. The assertion is valid as $\chi\to 0$ by (i) of Lemma 3, so we must prove that it remains valid for $\chi>0$. The proof is by contradiction. Assume that there exists $X^*$, $0<X^*<\infty$, such that at $\chi=X^*$,

$$I_0(X^*)/I_1(X^*)=y(X^*). \tag{C6}$$

If (C6) occurs more than once, then let $X^*$ be the smallest positive value at which (C6) is valid. Comparing (iii) of Lemma 3 with (C5) shows that

$$\frac{d}{d\chi}\left(\frac{I_0}{I_1}\right)=0\quad \text{at } \chi=X^*. \tag{C7}$$

But $I_0(\chi)/I_1(\chi)>y(\chi)$ for $\chi<X^*$, so $I_0(\chi)/I_1(\chi)$ must intersect $y(\chi)$ from *above* at $\chi=X^*$, and $y(\chi)$ is a decreasing function, so if $I_0(\chi)/I_1(\chi)$ intersects $y(\chi)$ from above at $\chi=X^*$, then necessarily

$$\frac{d}{d\chi}\left(\frac{I_0}{I_1}\right)<0\quad \text{at } \chi=X^*.$$

This contradicts (C7), so there can be no such point $X^*$, and Lemma 4 holds for all $\chi>0$.

## APPENDIX D: THE COEFFICIENTS IN (41)

*Lemma 5:* $\alpha(\chi)>0$ for $0<\chi<\infty$.

*Proof:* From (41a),

$$\alpha(\chi)=\left(\frac{\chi I_0}{I_1}\right)\left[\left(\frac{\chi I_0}{I_1}\right)-1\right]-\chi^2. \tag{D1}$$

From Lemma 4,

$$\left(\frac{\chi I_0}{I_1}\right)-1>\frac{1}{2}+\sqrt{\frac{1}{4}+\chi^2}-1>0\quad \text{for } \chi>0.$$

Using Lemma 4 again shows that for $\chi>0$,

$$\alpha(\chi)>[\tfrac{1}{2}+\sqrt{\tfrac{1}{4}+\chi^2}]\cdot[-\tfrac{1}{2}+\sqrt{\tfrac{1}{4}+\chi^2}]-\chi^2. \tag{D2}$$

The right-hand side of (D2) is identically zero, so this establishes Lemma 5.

*Lemma 6:* As $\chi\to 0$, $\alpha(\chi)\to 2$.

*Proof:* Use (41a) and (i) of Lemma 3.

*Lemma 7:* With $\beta(\chi,\nu m^2/\tau)$ and $\alpha(\chi)$ defined in (41),

$$\beta\left(\chi,\frac{\nu m^2}{\tau}\right)-\alpha(\chi)>0 \quad \text{for } \chi>0, \quad \frac{\nu m^2}{\tau}\geqslant 0.$$

*Proof:* From (41), we may write

$$\beta-\alpha=T_1(\chi)+\left(\frac{2\nu m^2}{\tau}\right)\left[\left(\frac{\chi I_0}{I_1}\right)-\chi^2-1\right], \tag{D3}$$

where

$$T_1(\chi)=3\left(\frac{\chi I_0}{I_1}\right)^3-8\left(\frac{\chi I_0}{I_1}\right)^2+5\left(\frac{\chi I_0}{I_1}\right)-3\chi^2\left(\frac{\chi I_0}{I_1}\right)+5\chi^2.$$

From Lemma 4, for $\chi>0$,

$$\left[\left(\frac{\chi I_0}{I_1}\right)-\chi^2-1\right]>\left[\left(\frac{1}{2}+\sqrt{\frac{1}{4}+\chi^2}\right)^2-\chi^2-1\right]=\left[\sqrt{\tfrac{1}{4}+\chi^2}-\tfrac{1}{2}\right]>0.$$

Meanwhile, $T_1(\chi)$ can be factored:

$$T_1(\chi)=\left[3\left(\frac{\chi I_0}{I_1}\right)-5\right]\left[\left(\frac{\chi I_0}{I_1}\right)^2-\left(\frac{\chi I_0}{I_1}\right)-\chi^2\right]. \tag{D4}$$

Comparing with (D1) shows that the second factor in (D4) is $\alpha(\chi)$, so by Lemmas 5 and 6 it is positive for $\chi\geqslant 0$.

To show that the first factor in (D4) is positive, define

$$T_2(\chi)=\left(\frac{\chi I_0}{I_1}\right)-\frac{5}{3}.$$

It follows from (i) of Lemma 3 that as $\chi\to 0$, $T_2(\chi)\to 1/3>0$. We need to show that $T_3(\chi)>0$ for all $\chi>0$. Use (iii) of Lemma 3, plus algebra, to show that

$$\frac{dT_2}{d\chi}=\chi+\frac{5}{9\chi}-\frac{(T_2)^2}{\chi}-\frac{4(T_2)}{3\chi}. \tag{D5}$$

Now mimic the proof of Lemma 4. Assume that there exists $X^*$, with $0<X^*<\infty$, such that at $\chi=X^*$,

$$T_2(X^*)=0. \tag{D6}$$

If (D6) occurs more than once, then let $X^*$ be the smallest positive value at which (D6) is valid. At $\chi=X^*$, $dT_2/d\chi>0$ from (D6). But $T_2(\chi)>0$ for $\chi<X^*$, so this plus (D6) assures that

$$\frac{dT_2}{d\chi}\leqslant 0 \quad \text{at } \chi=X^*.$$

This is a contradiction, so there can be no such point $X^*$. Therefore $T_2(\chi)>0$ for all $\chi\geqslant 0$. Therefore both factors in (D4) are positive for $\chi\geqslant 0$, so $T_1(\chi)>0$. Therefore both terms in (D3) are positive for $\chi>0$, $\nu m^2/\tau\geqslant 0$. This completes the proof.

*Lemma 8:* As $\chi\to 0$ and $m\to 0$, $\beta-\alpha\to 2$.

*Proof:* This follows from (D3), (D4), and (i) of Lemma 3.


[1] J. Eggers, ''Universal pinching of 3D axisymmetric free-surface flow,'' Phys. Rev. Lett. **71**, 3458 (1993).
[2] X. D. Shi, M. P. Brenner, and S. R. Nagel, ''A cascade of structure in a drop falling from a faucet,'' Science **265**, 219 (1994).
[3] M. P. Brenner, X. D. Shi, and S. R. Nagel, ''Iterated instabilities during droplet fission,'' Phys. Rev. Lett. **73**, 3391 (1994).
[4] X. Zhang and O. A. Basaran, ''An experimental study of dynamics of drop formation,'' Phys. Fluids **7**, 1184 (1995).
[5] D. M. Henderson, W. G. Pritchard, and L. B. Smolka, ''On the pinch-off of a pendant drop of viscous fluid,'' Phys. Fluids A **9**, 3188 (1997).
[6] D. H. Peregrine, G. Shoker, and A. Symon, ''The bifurcation of liquid bridges,'' J. Fluid Mech. **212**, 25 (1990).
[7] J. Eggers, ''Theory of drop formation,'' Phys. Fluids **7**, 941 (1995).
[8] S. E. Bechtel, C. D. Carlson, and M. G. Forest, ''Recovery of the Rayleigh capillary instability from slender 1-D inviscid and viscous models,'' Phys. Fluids A **7**, 2956 (1995).
[9] R. M. S. M. Schulkes, ''The contraction of liquid filaments,'' J. Fluid Mech. **309**, 277 (1996).
[10] J. B. Keller and M. K. Miksis, ''Surface tension driven flows,'' SIAM (Soc. Ind. Appl. Math.) J. Appl. Math. **43**, 268 (1983).
[11] H. A. Stone, B. J. Bentley, and L. G. Leal, ''An experimental study of transient effects in the breakup of viscous drops,'' J. Fluid Mech. **173**, 131 (1986).
[12] J. Plateau, *Statique Expérimentale et Théoretique des Liquides Soumis aux Seules Forces Moléculaire* (Gauthier-Villars, Paris, 1873).
[13] Lord Rayleigh, ''On the instability of jets,'' Proc. London Math. Soc. **10**, 4 (1879).
[14] Lord Rayleigh, ''On the instability of a cylinder of viscous liquid under capillary force,'' Philos. Mag. **34**, 145 (1892).
[15] S. Chandrasekhar, *Hydrodynamic and Hydromagnetic Stability* (Dover, New York, 1961), especially Chap. 12,
[16] I. Frankel and D. Weihs, ''Stability of a capillary jet with linearly increasing axial velocity,'' J. Fluid Mech. **155**, 289 (1985).
[17] I. Frankel and D. Weihs, ''Influence of viscosity on the capillary instability of a stretching jet,'' J. Fluid Mech. **185**, 361 (1987).
[18] G. K. Batchelor, *An Introduction to Fluid Dynamics* (Cambridge University Press, Cambridge, 1967).
[19] S. Tomotika, Proc. R. Soc. London, Ser. A **153**, 302 (1936).
[20] E. L. Ince, *Ordinary Differential Equations* (Dover, New York, 1944), especially Chap. 10.
[21] G. Hellwig, *Differential Operators of Mathematical Physics* (Addison–Wesley, Palo Alto, CA, 1964).
[22] F. Bowman, *Introduction to Bessel Functions* (Dover, New York, 1958).
[23] M. Abramowitz and I. A. Stegun, *Handbook of Mathematical Functions* (USGPO, Washington, DC, 1964).
[24] J. Scoria, W. K. Chiu, and M. P. Norton, ''A study of unsteady laminar boundary layer flow on a flat plate using a smoke-wire/silhouette flow visualization technique,'' Exp. Therm. Fluid Sci. **3**, 291 (1990).
[25] C. M Bender and S. A. Orszag, *Advanced Mathematical Methods for Scientists and Engineers* (McGraw–Hill, New York, 1978).
[26] E. T. Whittaker and G. N. Watson, *A Course in Modern Analysis* (Cambridge University Press, London, 1980).